Letter

Strain-driven structural selection and amorphization during first-order phase transitions in nanocrystalline Ho_2O_3 under pressure

Xiaozhi Yan,[1,2,*] Xiangting Ren,[1,*] Shengcai Zhu,[3] Derrick Van Gennep,[2] Liping Wang,[1] Yusheng Zhao,[1] and Shanmin Wang[1,†]

[1]*Department of Physics and Academy for Advanced Interdisciplinary Studies, Southern University of Science and Technology, Shenzhen, Guangdong 518055, China*

[2]*Lyman Laboratory of Physics, Harvard University, Cambridge, Massachusetts 02138, USA*

[3]*School of Materials, Sun Yat-sen University, Guangzhou, Guangdong 510275, China*

(Received 17 October 2019; revised 5 March 2021; accepted 6 April 2021; published 15 April 2021)

Pressure-induced first-order phase transition often involves spatial disruption around the nucleus of a new phase, due to the inherent volume change. Atomic relaxations during this process produce lattice strain that in turn affects the nucleation kinetics and dynamics of transition, especially in nanoparticles. However, it is difficult to experimentally measure the lattice strain of materials, leading to many unsettled questions regarding size-dependent phenomena in nanomaterials at pressure. Here we present a method to determine the lattice strain of nanoparticles during first-order phase transitions using the pressure-volume data. A case study of nano-Ho_2O_3 with multiple pressure-induced phase transitions is systematically performed to reveal the critical role of lattice strain in the size-dependent phase selection and amorphization. A phenomenological model is also given to describe the metastability of intermediate phases and size-tunable phase evolution during the nucleation of new phases at pressure.

DOI: 10.1103/PhysRevB.103.L140103

I. INTRODUCTION

Studies of the first-order phase transition in nanocrystalline materials at pressure (P) have discovered many unprecedented phenomena and numerous new phases [1–4]. In a microscopic view, the first-order structural transition at pressure proceeds via a nucleation mechanism by which small nuclei of a new phase form under given conditions, but unless their sizes exceed a critical value (i.e., critical nucleus) they tend to dissolve rather than grow [5–10]. The critical nucleus size for most materials is a few to tens of nanometers [9,11,12], indicating that, in small nanocrystals, the phase transition may be completely retarded because of the confined volume that does not allow forming stable nuclei [11]. Although this simple picture is seemingly effective in explaining pressure-induced amorphization in ultrafine nanoparticles [11,13], interpretations for size-tunable phenomena associated with pressure-induced first-order phase transitions still remain ambiguous, including phase selection [14,15], phase stability enhancement [3,12,16], nucleation dynamics [11,17], and lattice anomalies [18–20].

By introducing surface energy (or surface tension) into the conventional thermodynamic models, only heuristic explanations on some size-dependent behaviors have been achieved, such as the proposed $1/r$ drop-off in transition pressure [16,21] and the surface-modification-induced phase selection at pressure [14,22,23]. In fact, these models would be more suitable for small nanoparticles with a crystallite size close to that of a critical nucleus of the high-P new phase, because the interfacial surface of the nucleus would largely overlap with the nanoparticle's surface shell and the surface tension can immediately exert the nucleus to govern the thermodynamics and kinetics of nucleation. However, for larger nanoparticles, the relatively small nuclei are formed within each nanoparticle and the nucleation kinetics is primarily determined by the interfacial surface, rather than the nanoparticle's surface shell. Thus, the surface effect on nucleation may not work in a straightforward manner, calling into question the adequacy of conventional models for nanomaterials.

A prominent feature of pressure-induced first-order phase transitions is the volume reduction (i.e., volume discontinuity), a disruptive process that induces complex atomic relaxations and motions as collectively manifested by lattice strain [10,24]. Lattices of both the involved low-P and high-P phases are slightly expanded relative to their equilibrium states, resembling the tensile-like macrostrain (only the compression process is considered for simplicity). Such defined strain represents an average displacement of atoms from their equilibrium positions. The strain is energetically unfavorable for phase transition and partially contributes to the transition hysteresis. In contrast to the bulk counterpart, the nanoparticle has a limited number of atoms involved in the relaxation process, resulting in a dramatic increase of lattice deformation. By means of the deformation, the surface tension can also be transmitted to nuclei by surface relaxations during transition, because the surface shell is highly strained and its relaxation will modify the strain state of nuclei. Remarkably,

*These authors contributed equally to this work.
†Corresponding author: wangsm@sustech.edu.cn

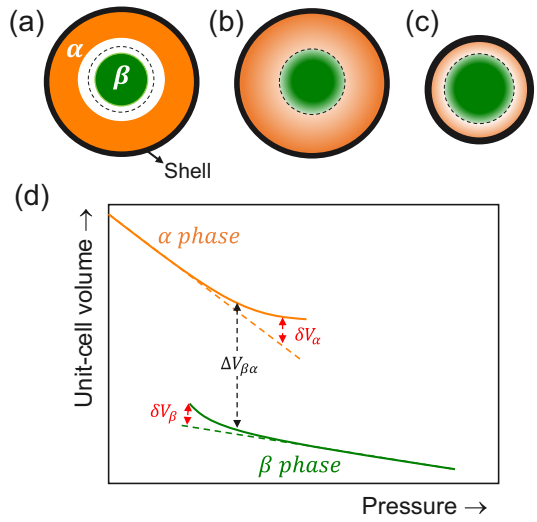

FIG. 1. Origin of lattice strain. (a) Formation of a single β nucleus within the parent α matrix in ideal equilibrium states without involving strain. A void layer corresponds to the volume reduction. (b) Relaxing lattices of both phases to produce strain (gradient color). (c) Reduced nanoparticle with a larger critical nucleus. The black bold lines and black dashed lines in (a)–(c) denote the surface shell and interfacial surface, respectively. (d) P-V data for both phases. The solid and dashed lines denote the observed trend lines and equilibrium P-V lines defined by their EoS, respectively.

the lattice strain is a secret ingredient linking to the surface tension and is crucial for understanding the dynamics and kinetics of nucleation. However, the influence of lattice strain on phase transition in nanocrystals has not been adequately addressed because of experimental difficulties in quantifying the strain effect, which has led to many ambiguities in this research field.

To assess the lattice strain of a pressure-induced first-order transition, a protocol is established in Fig. 1. Schematic diagrams of nucleating β phase within parent α matrix in Figs. 1(a)–1(c) illustrate the origin of strain, assuming that both phases are in spherical shapes and the transition proceeds through nucleation of a single nucleus for simplicity. Because the nanoparticle's core is often nearly defect free [25,26], the β nucleus is preferably formed via a homogeneous nucleation. In an ideal equilibrium process of transformation [Fig. 1(a)], nucleating β in the α phase would produce a void space between them, due to the volume reduction. As such, the system becomes unstable and the relaxations of atoms generate lattice strain in both phases [Fig. 1(b)]. Besides, reducing the nanoparticle size increases the thus-produced strain, hence an increase of the critical nucleus size [Fig. 1(c)] [11,27]. A strategy for deriving the strain from pressure-volume (P-V) data is shown in Fig. 1(d). A volume reduction, $\frac{V_\beta - V_\alpha}{V_\alpha} = \frac{\Delta V_{\beta\alpha}}{V_\alpha}$, is expected, where V_α and V_β are their cell volumes and $\Delta V_{\beta\alpha}$ represents the volume difference. In the phase coexisting region, the volumes deviate from their respective P-V curves as denoted with δV_α and δV_β.

Considering β has a volume of nV_β, the strain stored in both phases can be quantified by strain energy densities of $\Delta E_\alpha = \frac{P\cdot(m\delta V_\alpha)}{nV_\beta}$ and $\Delta E_\beta = \frac{P\cdot(n\delta V_\beta)}{nV_\beta}$ [24], respectively, where m and n represent numbers of unit cells for the formed β and the remaining α. The total strain energy density ($\Delta E_{\beta\alpha}$) of the system is

$$\Delta E_{\beta\alpha} = \Delta E_\alpha + \Delta E_\beta = \frac{\eta}{1-\eta}\frac{P\cdot\delta V_\alpha}{V_\alpha} + \frac{P\cdot\delta V_\beta}{V_\beta}, \quad (1)$$

where η denotes the volume fraction of α phase (thus, $\frac{mV_\alpha}{nV_\beta} = \frac{\eta}{1-\eta}$). However, for the β phase, its volume deviation is difficult to determine because the phase fraction is often not sufficient for a reliable measurement. Instead, ΔE_β can be calculated by analysis of α, provided that pressures on both phases is identical. Accordingly, the volume deviation of β can be calculated by

$$B_\beta\frac{\delta V_\beta}{V_\beta} = \Delta P_\beta = \Delta P_\alpha = P - P_{\rm calc}, \quad (2)$$

where ΔP_α and ΔP_β denote pressure changes, and P and $P_{\rm calc}$ are pressures determined using a marker and calculated using the equation of state (EoS) of α phase, respectively. Bulk modulus (B_β) of β is derived from its P-V data [Fig. 1(d)]. To explore the strain effect on phase transition in nanomaterials, a case study of nano-Ho_2O_3 with pressure-induced multiple phase transitions is performed to examine size-dependent phase evolution. Experimental details are given in the Supplemental Material [28].

II. RESULTS AND DISCUSSION

Similar to most rare-earth sesquioxides [29], Ho_2O_3 has three known structural modifications: cubic, monoclinic, and hexagonal phases [Fig. 2(a)] [30,31], denoted hereinafter as α, β, and γ, respectively. The α and γ phases are six- and sevenfold coordinated, respectively, while the intermediate β has a mixed coordination (Fig. S2). In the bulk sample [Fig. 2(b)], the $\alpha\rightarrow\beta$ and $\beta\rightarrow\gamma$ transitions start ~10.3 and 14.9 GPa, respectively, which agree well with high-P Raman measurements (Fig. S3). Both the high-P phases can coexist up to 38.6 GPa (Fig. S4 and Table S1), consistent with earlier reports [30]. Such a structural transition sequence can be interpreted in terms of the Peierls distortion associated with bond reorderings [Fig. 2(a)], similar to what occurred in many binary semiconductors (e.g., CdSe) [9,32]. Apparently, pressure drives the system toward more ordered structures.

In nanoparticles, the $\alpha\rightarrow\beta$ transition is suppressed [Figs. 2(c)–2(d)], mainly because the nucleation can be kinetically hindered in the confined volume of small grains. Instead, γ-Ho_2O_3 formed directly from α phase with the absence of intermediate β. As the particle size is reduced from 43 to 14 nm, the onset pressure for the formation of γ phase increases from 12.4 to 14.8 GPa, demonstrating extended stability of α-Ho_2O_3. Similar size-dependent phase stability was observed in other systems [3,12,16]. On the other hand, γ-Ho_2O_3 occurred directly from α in nanoparticles at lower pressures than that in the bulk sample (~14.9 GPa), which can be explained by the Ostwald step rule [5,8,33–35], which states the new phase often nucleates from a metastable intermediate phase rather than its thermodynamically stable parent phase to lower the kinetic barrier for the phase transition. Thus, although β-Ho_2O_3 is absent in nanoparticles, the γ

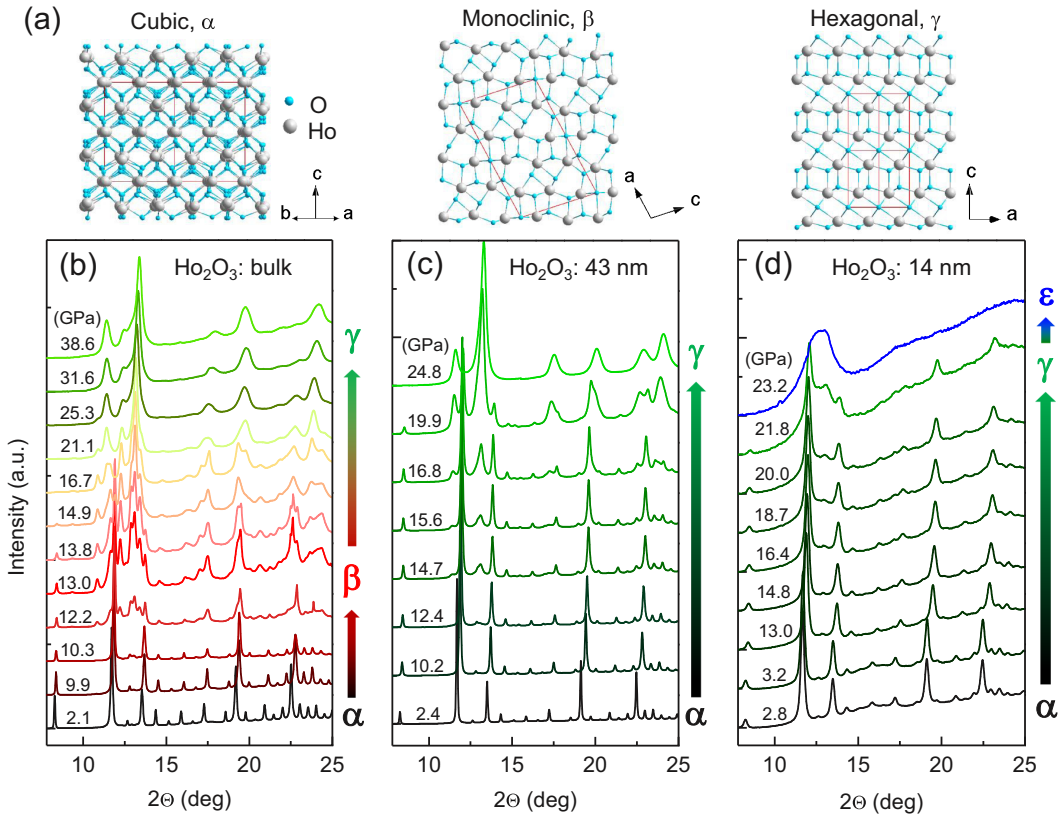

FIG. 2. Structures and high-P x-ray diffraction (XRD) measurements. (a) Structures of Ho_2O_3 polymorphs. (b)–(d) High-P XRD patterns for samples with different sizes.

phase would still preferably nucleate from β embryos as an intermediate step [36–38]. Note that these β embryos can only occur dynamically and hardly be probed by ordinary x-ray diffraction (XRD) measurements; they may be in a cluster form (β^*) and structurally similar to that of β phase. As the particle size decreases down to 14 nm [Fig. 2(d)], only a weak 101 peak of γ-Ho_2O_3 is identifiable (Fig. S5) and is fully merged into a broad hump at 23.2 GPa [Figs. 2(d) and S6], signaling a complete amorphization. The amorphous phase can be preserved to ambient pressure, in contrast to that for the bulk and 43-nm samples with β-Ho_2O_3 as a recovered product (Fig. S7), indicating complicated transition kinetics during decompression.

The underlying mechanism of structural selection in nano-Ho_2O_3 during compression can be understood by considering the strain effect. Figure 3(a) shows the P-V data derived from those high-P XRD data. The volumes of α and β are normalized to that of γ-Ho_2O_3 according to their molar volumes, respectively. A large volume reduction, $\frac{\Delta V_{\beta\alpha}}{V_\alpha} \approx -8.6\%$, is observed for the $\alpha \rightarrow \beta$ transition in the bulk sample, while a smaller value of $\frac{\Delta V_{\gamma\beta}}{V_\beta} \approx -1.4\%$ for the $\beta \rightarrow \gamma$ transition. In the 43-nm sample, due to the absence of a β phase the direct $\alpha \rightarrow \gamma$ transition has a ~8.5% volume drop.

A close look at the P-V data of α-Ho_2O_3 in Figs. 3(b)–3(c) reveals volume deviations from their EoS trend lines, especially in nanocrystals, suggesting the strain is produced during transition. Using Eq. (1), the total strain energy is quantitatively calculated and shown in Fig. 3(d). In the bulk sample, the strain energy is close to zero, except for a slight increase during transition. Remarkably, the strain energy in nanoparticles is substantially increased to ~6 kJ/mol and ~22 kJ/mol for the 43-nm and 14-nm samples, respectively, which are comparable with enthalpy change during transition, i.e., $\Delta P \cdot (-\Delta V_{\beta\alpha}) \approx 20$ kJ/mol (the pressure overstep, ΔP, can be estimated from transition hysteresis [9]). Unambiguously, in nanoparticles the strain is large enough to influence the nucleation of phase transition.

In fact, pressure-induced multiple phase transitions in materials are often concurrent in a narrow pressure range (e.g., Ho_2O_3 in Fig. 2 and other systems [15,42]), suggesting their nucleation processes are substantially overlapped. To properly describe the phase evolution, we rewrite the activation energy, ΔG, of the system involving nucleation of multiple phases by

$$\Delta G = \sum \Delta G_{ji} = \Delta G_{\beta\alpha} + \Delta G_{\gamma\beta} + \Delta G_{\varepsilon\gamma} + \cdots . \quad (3)$$

Here ΔG_{ji} ($j = \beta, \gamma, \varepsilon, \ldots; i = \alpha, \beta, \gamma, \ldots$) denotes the free energy change for each transition; assuming the Ostwald step rule holds for the transition sequence so as to lower the interfacial energy (σ_{ij}). New phases β, γ, and ε nucleate from the corresponding parent metastable phases (or dynamically occurring embryos) with nucleus radii denoted with r_β, r_γ, and r_ε, respectively. These multiple phase transitions are mutually correlated via their relative nucleus sizes and interfacial energies. Thus, Eq. (3) can be

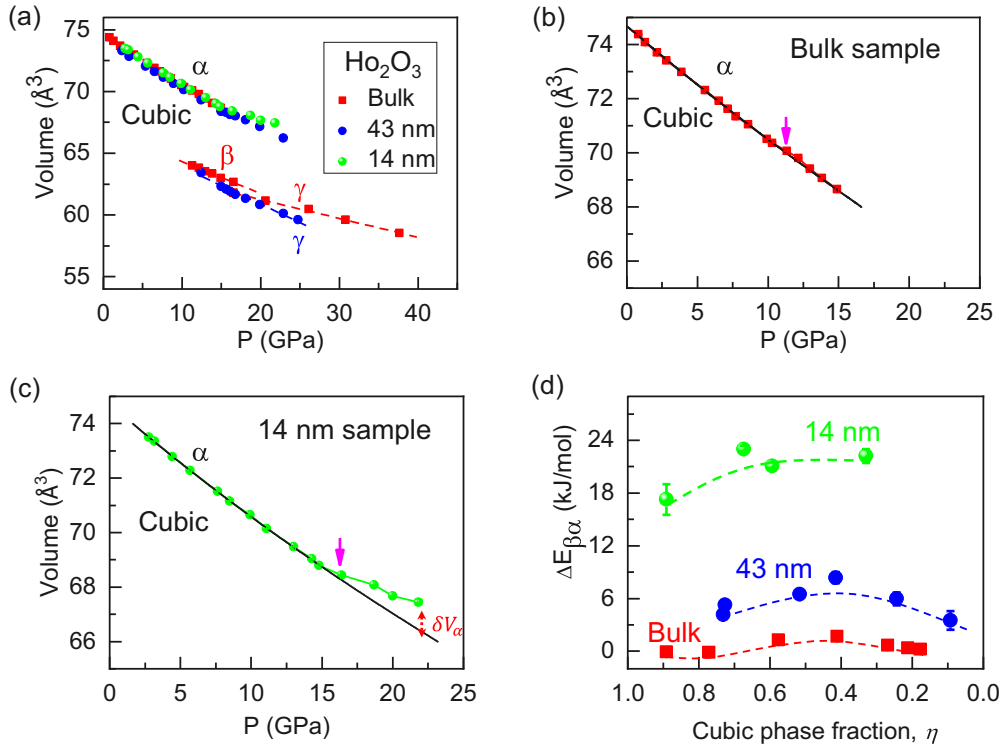

FIG. 3. P-V data and strain energy density. (a) Observed P-V data. (b)–(c) P-V data for both the bulk and 14-nm α-Ho_2O_3, respectively. The solid black line in each panel represents a fit of low-P data to a Birch-Murnaghan EoS (Fig. S8 and Table S2) [30,39–41]. Magenta arrows in (b) and (c) denote the onset of volume deviations. The case of 43-nm sample is presented in Fig. S9. In (a)–(c), the error bars are too small to show. (d) Derived $\Delta E_{\beta\alpha}$ vs η (see Fig. S10 for ΔE_α vs η).

specified as

$$\Delta G = \tfrac{4}{3}\pi r_\beta^3(\Delta U_{\beta\alpha} - T\Delta S_{\beta\alpha} + P\Delta V_{\beta\alpha} - \Delta E_{\beta\alpha}) + 4\pi r_\beta^2\sigma_{\beta\alpha} + \tfrac{4}{3}\pi r_\gamma^3(\Delta U_{\gamma\beta} - T\Delta S_{\gamma\beta} + P\Delta V_{\gamma\beta} - \Delta E_{\gamma\beta}) + 4\pi r_\gamma^2\sigma_{\gamma\beta} + \tfrac{4}{3}\pi r_\varepsilon^3(\Delta U_{\varepsilon\gamma} - T\Delta S_{\varepsilon\gamma} + P\Delta V_{\varepsilon\gamma} - \Delta E_{\varepsilon\gamma}) + 4\pi r_\varepsilon^2\sigma_{\varepsilon\gamma}. \quad (4)$$

For each transition, around its equilibrium transition pressure (P_{ji}^0), the changes in internal energy density (ΔU_{ji}) and entropy density (ΔS_{ji}) are negligible relative to those in strain energy (ΔE_{ji}) and work-done term ($P\Delta V_{ji}$). Expanding each that is bracketed in Eq. (4) to first order in ($P-P_{ji}^0$) and performing the maximization yields a critical diameter (i.e., $d_j^* = 2r_j^*$),

$$d_j^* \approx \frac{4\sigma_{ji}}{(P - P_{ji}^0)(-\Delta V_{ji}) - \Delta E_{ji}} (j = \beta,\ \gamma, \varepsilon; i = \alpha, \beta, \gamma). \quad (5)$$

The kinetic barrier height is

$$\Delta G_{ji}^*(d_j^*) = \tfrac{1}{3}\pi d_j^{*2}\sigma_{ji}, \quad (6)$$

where ($P-P_{ji}^0$) and ΔV_{ji} represent the pressure overstep required to drive phase transition and the volume reduction (i.e., $\Delta V_{ji} < 0$), respectively; they are nearly constant regardless of the particle size. The strain energy (ΔE_{ji}) increases with reducing size, leading to rapid increases in both d_j^* and ΔG_{ji}^*. Apparently, the surface tension of a nanoparticle is not included in Eq. (4), but it can be transmitted by lattice relaxations during phase transition. Thus, the size effect on nucleation is mainly active through the lattice strain. If the required critical nucleus size exceeds that of its parent phase, formation of the new phase is kinetically suppressed; instead, the new phase embryos or clusters would occur dynamically, which ultimately dissolve into a more stable state.

To explore the nucleation kinetics in nano-Ho_2O_3, we derived the domain size for all the involved phases from XRD peak broadening, using the Scherrer formula (Fig. 4). In the bulk sample, the size of α-Ho_2O_3 is rapidly reduced from ~200 to 25 nm during transition, while the domain size of β is ~18 nm, implying that the $\alpha \rightarrow \beta$ transition undergoes a multiple-nucleation process [Fig. 4(a)]. No grain growth is observed for β-Ho_2O_3 as it is kinetically difficult in solids at room temperature, indicating its critical nucleus size of $d_\beta^* \approx 18$ nm. Clearly, γ-Ho_2O_3 nucleates within the preformed β through a single-nucleation process with a critical size of $d_\gamma^* \approx 15$ nm.

In the 43-nm sample [Fig. 4(b)], the absence of β is mainly due to markedly increased strain (i.e., $\Delta E_{\beta\alpha} \approx 6$ kJ/mol) that should increase the required d_β^* over the nanoparticle size (~43 nm), according to Eq. (5). Therefore, only an embryo form of β-Ho_2O_3 would occur at the early stage of nucleating γ-Ho_2O_3, and the thus-obtained critical nucleus size of γ-Ho_2O_3 is $d_\gamma^* \approx 15$ nm, similar to that in the bulk sample. This further confirms γ-Ho_2O_3 should form from β embryos

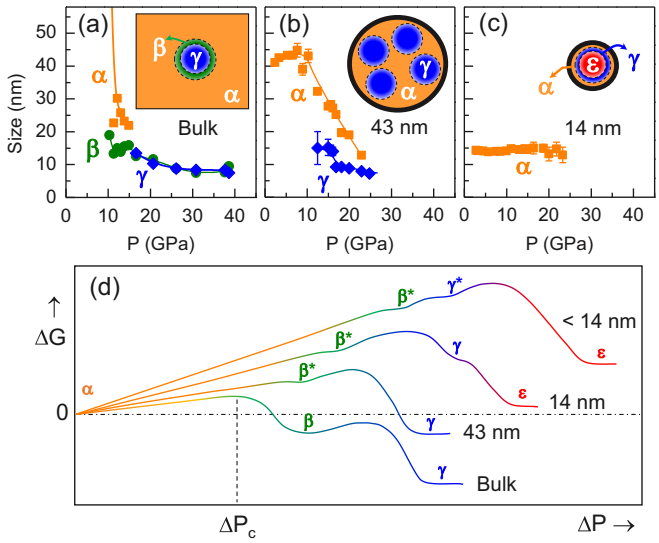

FIG. 4. Evolutions of crystallite size and free energy landscape of pressure-induced multiple phase transitions in nano-Ho_2O_3. (a)–(c) Domain sizes vs pressure for the involved phases of Ho_2O_3 with various starting nanoparticle sizes. Inset in each panel schematically illustrates nucleation of new phases. (d) Conceptual illustration of size-dependent energy landscapes against the pressure overstep ΔP, in terms of Eq. (5). In each line, the overall energy maximum occurs at a critical pressure (ΔP_c), above which high-P phases start to nucleate, as manifested by large energy minima. While the formation of these phases would be suppressed with decreasing nanoparticle size. Instead, according to the Ostwald step rule, these phases would occur dynamically in their embryo forms (i.e., β^* and γ^*) below the critical pressure for nucleating more stable high-P phases.

with an interfacial energy $\sigma_{\gamma\beta}$ as nearly identical as that occurred in the bulk sample for producing the γ nucleus with a similar critical size. Meanwhile, the size of the α phase decreases with increasing pressure in this sample, likely due to the increase of γ nucleus number (i.e., a multinucleation process). In Fig. 4(c), the γ phase of the 14-nm sample occurs on the border of amorphization at ~21.8 GPa, indicating the critical nucleus is close to 14 nm; the appreciably increased strain would lead to dynamically occurring β embryos for nucleating γ-H_2O_3. Further decrease of nanoparticle size (d) below the required d^*_γ, a direct amorphization is expected at higher pressure, as reported in 6-nm TiO_2 [13]. The pristine α-H_2O_3 may also become amorphous even at ambient pressure, if its crystallite size is below a critical size, which explains what is observed in 3-nm PbTe [17].

Based on Eq. (5), variations of free energy during multiple phase transitions can be tentatively depicted in Fig. 4(d) with a number of energy minima and barriers. The energy landscape of bulk sample is mainly characterized with a prominent barrier (i.e., the overall energy maximum) between the original and high-P phases. Pressure increases metastability of α-Ho_2O_3 and fluctuates its lattice to overcome the energy barrier, leading to the nucleation of critical β nucleus. This concept is commonly accepted in the conventional nucleation theories [5–8,38,43,44]. In the bulk sample, the most stable γ phase must nucleate from the intermediate β, because the involved interfacial energy is much lower than that of direct nucleation of γ within α (i.e., $\sigma_{\gamma\beta} < \sigma_{\beta\alpha}$), obeying the Ostwald step rule [5,8].

Reducing the nanoparticle size appreciably increases lattice strain, which greatly modifies the energy landscapes during nucleating high-P phases [Fig. 4(d)]. For example, the most stable γ-Ho_2O_3 becomes a metastable intermediate for forming amorphous phase in the 14-nm sample [Fig. 2(d)]. By tuning the nanoparticle size (hence, the strain), the phase stability can be completely altered, and all crystalline phases may be kinetically suppressed in their embryo forms at the early stage of nucleation for phase transition. Recently, a renewed theory called the generalized Ostwald step rule was given to illustrate phase evaluation during nucleating critical nucleus [5]. By simply extending this rule to the embryoforming stage of nucleation, the size-tunable phase selection in nano-Ho_2O_3 can be well understood. We thus argue that the dynamics of nucleation at the early stage is vital to understanding pressure-induced multiple phase transitions.

For the $\gamma \rightarrow \varepsilon$ amorphous transition, the entropy change may be decisive to initiate transition by a different mechanism (e.g., a meltinglike process [45]). In ultrafine nanoparticles, the surface modification is also important for phase selection and amorphization as reported in TiO_2 [14,22] and ZnS [23], because the modified surface tension can greatly alter the lattice strain through atomic relaxations during nucleation. In addition, using our model, many previously unsettled phenomena associated with pressure-induced phase transitions in nanomaterials can be excellently interpreted, including amorphizations in 6-nm TiO_2 [11,13,46], 16-nm Y_2O_3 [15], 5-nm PbTe [17], and Bi_2O_3 [47] and the lattice or modulus anomalies in CeO_2 [19,20], ZnO [48], Ge [18], and Fe [49] across phase transitions at pressures. Lastly, our model can also be used to help understand some important phase transitions under high P-T conditions, such as transformations of graphite → diamond and hBN → cBN with hexagonal and wurtzite phases as intermediates, respectively [42,50,51].

III. CONCLUSIONS

In summary, a simple pressure-volume method is formulated for determining the lattice strain produced during the pressure-induced first-order phase transitions. Applying this method to nano-Ho_2O_3 with multiple phase transitions at pressures, we find that the strain energy in nanocrystals is appreciably large, which leads to the significant increase of the critical nucleus and kinetic barrier for retarding nucleation of high-P phases, resulting in structural selection or amorphization. A phenomenological model is established from an energy perspective to explore the size-dependent phase evolution, which can be well understood by extending the generalized Ostwald step rule to the early stage of nucleation. Our findings can be used for addressing many unsettled size-dependent phenomena associated with first-order phase transitions.

ACKNOWLEDGMENTS

We gratefully acknowledge funding support from the National Natural Science Foundation of China (Grant No. 11027405), the Key Research Platforms and Research

Projects of Universities in Guangdong Province (Grant No. 2018KZDXM062), the Guangdong Innovative & Entrepreneurial Research Team Program (Grant No. 2016ZT06C279), the Shenzhen Peacock Plan (Grant No. KQTD2016053019134356), the Shenzhen Development and Reform Commission Foundation for Shenzhen Engineering Research Center for Frontier Materials Synthesis at High Pressure, the Shenzhen Science and Technology Innovation Committee (Grant No. JCYJ20190809173213150), and the Research Platform for Crystal Growth & Thin-Film Preparation at SUSTech. High-P synchrotron XRD measurements were performed at the 4W2 beamline of BSRF and the BL15U1 beamline of SSRF.

X.Z.Y. and S.M.W. conceived the project. X.Z.Y., X.T.R., L.P.W., and D.V.G. performed high-P synchrotron XRD and Raman measurements. X.Z.Y., S.C.Z., and S.M.W. did data analysis. S.M.W., X.Z.Y., L.P.W., D.V.G., and Y.S.Z. wrote the manuscript. All authors contributed to interpretation of the data.

The authors declare no competing interests.

[1] H.-K. Mao, X.-J. Chen, Y. Ding, B. Li, and L. Wang, Rev. Mod. Phys. **90**, 015007 (2018).
[2] F. Bai, K. Bian, X. Huang, Z. Wang, and H. Fan, Chem. Rev. **119**, 7673 (2019).
[3] D. Machon, V. Pischedda, S. Le Floch, and A. San-Miguel, J. Appl. Phys. **124**, 160902 (2018).
[4] A. P. Alivisatos, J. Phys. Chem. **100**, 13226 (1996).
[5] J. W. P. Schmelzer and A. S. Abyzov, in *Thermal Physics and Thermal Analysis: From Macro to Micro, Highlighting Thermodynamics, Kinetics and Nanomaterials*, edited by J. Šesták, P. Hubík, and J. J. Mareš (Springer International Publishing, Cham, 2017), p. 195.
[6] W. Sun, S. T. Dacek, S. P. Ong, G. Hautier, A. Jain, W. D. Richards, A. C. Gamst, K. A. Persson, and G. Hautier, Sci. Adv. **2**, e1600225 (2016).
[7] E. Pretti, H. Zerze, M. Song, Y. Ding, R. Mao, and J. Mittal, Sci. Adv. **5**, eaaw5912 (2019) .
[8] A. Navrotsky, Proc. Natl. Acad. Sci. USA **101**, 12096 (2004).
[9] U. D. Venkateswaran, L. J. Cui, B. A. Weinstein, and F. A. Chambers, Phys. Rev. B **45**, 9237 (1992).
[10] L. Zhang, L.-Q. Chen, and Q. Du, Phys. Rev. Lett. **98**, 265703 (2007).
[11] G. R. Hearne, in *High-Pressure Crystallography*, edited by E. Boldyreva, and P. Dera (Springer Netherlands, Dordrecht, 2010), p. 503.
[12] S. H. Tolbert and A. P. Alivisatos, Science **265**, 373 (1994).
[13] V. Pischedda, G. R. Hearne, A. M. Dawe, and J. E. Lowther, Phys. Rev. Lett. **96**, 035509 (2006).
[14] L. Piot, S. Le Floch, T. Cornier, S. Daniele, and D. Machon, J. Phys. Chem. C **117**, 11133 (2013).
[15] L. Wang, W. Yang, Y. Ding, Y. Ren, S. Xiao, B. Liu, S. V. Sinogeikin, Y. Meng, D. J. Gosztola, G. Shen, R. J. Hemley, W. L. Mao, and H.-K. Mao, Phys. Rev. Lett. **105**, 095701 (2010).
[16] D. Machon, L. Piot, D. Hapiuk, B. Masenelli, F. Demoisson, R. Piolet, M. Ariane, S. Mishra, S. Daniele, M. Hosni, N. Jouini, S. Farhat, and P. Mélinon, Nano Lett. **14**, 269 (2014).
[17] Z. Quan, Y. Wang, I.-T. Bae, W. S. Loc, C. Wang, Z. Wang, and J. Fang, Nano Lett. **11**, 5531 (2011).
[18] X. Yan, D. Tan, X. Ren, W. Yang, D. He, and H.-K. Mao, Appl. Phys. Lett. **106**, 171902 (2015).
[19] M. Y. Ge, Y. Z. Fang, H. Wang, W. Chen, Y. He, E. Z. Liu, N. H. Su, K. Stahl, Y. P. Feng, J. S. Tse, T. Kikegawa, S. Nakano, Z. L. Zhang, U. Kaiser, F. M. Wu, K. Mao, and J. Z. Jiang, New J. Phys. **10**, 123016 (2008).
[20] Q. Wang, D. He, F. Peng, L. Lei, P. Liu, S. Yin, P. Wang, C. Xu, and J. Liu, Sci. Rep. **4**, 4441 (2014).
[21] J.-F. Lin, H. Watson, G. Vanko, E. E. Alp, V. B. Prakapenka, P. Dera, V. V. Struzhkin, A. Kubo, J. Zhao, C. McCammon, and W. J. Evans, Nat. Geosci. **1**, 688 (2008).
[22] D. Machon, M. Daniel, P. Bouvier, S. Daniele, S. Le Floch, P. Melinon, and V. Pischedda, J. Phys. Chem. C **115**, 22286 (2011).
[23] H. Zhang, B. Gilbert, F. Huang, and J. F. Banfield, Nature (London) **424**, 1025 (2003).
[24] J. D. Eshelby and R. E. Peierls, Proc. R. Soc. London Ser. A **241**, 376 (1957).
[25] Z. Budrovic, H. Van Swygenhoven, P. M. Derlet, S. Van Petegem, and B. Schmitt, Science **304**, 273 (2004).
[26] V. G. Gryaznov, A. M. Kaprelov, and A. E. Romanov, Scr. Metall. **23**, 1443 (1989).
[27] R. E. Hanneman, M. D. Banus, and H. C. Gatos, J. Phys. Chem. Solids **25**, 293 (1964).
[28] See Supplemental Material at http://link.aps.org/supplemental/10.1103/PhysRevB.103.L140103 for details on experimental details, crystal structure refinements, high-pressure Raman measurements, and pressure-volume data of samples.
[29] N. Dilawar Sharma, J. Singh, A. Vijay, K. Samanta, S. Dogra, and A. K. Bandyopadhyay, J. Phys. Chem. C **120**, 11679 (2016).
[30] S. Jiang, J. Liu, X. Li, L. Bai, W. Xiao, Y. Zhang, C. Lin, Y. Li, and L. Tang, J. Appl. Phys. **110**, 013526 (2011).
[31] X. Yan, X. Ren, D. He, B. Chen, and W. Yang, J. Appl. Phys. **116**, 033507 (2014).
[32] S. H. Tolbert and A. P. Alivisatos, Annu. Rev. Phys. Chem. **46**, 595 (1995).
[33] S.-Y. Chung, Y.-M. Kim, J.-G. Kim, and Y.-J. Kim, Nat. Phys. **5**, 68 (2009).
[34] R. A. Van Santen, J. Phys. Chem. **88**, 5768 (1984).
[35] W. Ostwald, Z. Phys. Chem. **22U**, 289 (1897).
[36] P. Rein ten Wolde, M. J. Ruiz-Montero, and D. Frenkel, J. Chem. Phys. **104**, 9932 (1996).
[37] S. Auer and D. Frenkel, Nature (London) **409**, 1020 (2001).
[38] S. C. Hendy, Phys. Rev. B **71**, 115404 (2005).
[39] F. D. Murnaghan, Proc. Natl. Acad. Sci. USA **30**, 244 (1944).
[40] F. Birch, Phys. Rev. **71**, 809 (1947).
[41] R. J. Angel, Rev. Mineral. Geochem. **41**, 35 (2000).
[42] A. Yoshiasa, Y. Murai, O. Ohtaka, and T. Katsura, Jpn. J. Appl. Phys. **42**, 1694 (2003).
[43] J. F. Lutsko, Sci. Adv. **5**, eaav7399 (2019).
[44] K. Henzler, E. O. Fetisov, M. Galib, M. D. Baer, B. A. Legg, C. Borca, J. M. Xto, S. Pin, J. L. Fulton, G. K. Schenter, N. Govind, J. I. Siepmann, C. J. Mundy, T. Huthwelker, and J. J. De Yoreo, Sci. Adv. **4**, eaao6283 (2018).

[45] S. K. Deb, M. Wilding, M. Somayazulu, and P. F. McMillan, Nature (London) **414**, 528 (2001).

[46] V. Swamy, A. Kuznetsov, L. S. Dubrovinsky, P. F. McMillan, V. B. Prakapenka, G. Shen, and B. C. Muddle, Phys. Rev. Lett. **96**, 135702 (2006).

[47] A. L. J. Pereira, D. Errandonea, A. Beltrán, L. Gracia, O. Gomis, J. A. Sans, B. García-Domene, A. Miquel-Veyrat, F. J. Manjón, A. Muñoz, and C. Popescu, J. Phys.: Condens. Matter **25**, 475402 (2013).

[48] X. Yan, H. Dong, Y. Li, C. Lin, C. Park, D. He, and W. Yang, Sci. Rep. **6**, 24958 (2016).

[49] A. P. Jephcoat, H. K. Mao, and P. M. Bell, J. Geophys. Res. **91**, 4677 (1986).

[50] R. Z. Khaliullin, H. Eshet, T. D. Kühne, J. Behler, and M. Parrinello, Nat. Mater. **10**, 693 (2011).

[51] Y.-P. Xie, X.-J. Zhang, and Z.-P. Liu, J. Am. Chem. Soc. **139**, 2545 (2017).